NEUROSCIENCE

Transparent arrays of bilayer-nanomesh microelectrodes for simultaneous electrophysiology and two-photon imaging in the brain

Yi Qiang[1]*, Pietro Artoni[2]*, Kyung Jin Seo[1]*, Stanislav Culaclii[3], Victoria Hogan[2], Xuanyi Zhao[1], Yiding Zhong[1], Xun Han[1], Po-Min Wang[3], Yi-Kai Lo[3], Yueming Li[4], Henil A. Patel[5], Yifu Huang[6], Abhijeet Sambangi[1], Jung Soo V. Chu[1], Wentai Liu[3,7,8], Michela Fagiolini[2]†, Hui Fang[1,9]†

Transparent microelectrode arrays have emerged as increasingly important tools for neuroscience by allowing simultaneous coupling of big and time-resolved electrophysiology data with optically measured, spatially and type resolved single neuron activity. Scaling down transparent electrodes to the length scale of a single neuron is challenging since conventional transparent conductors are limited by their capacitive electrode/electrolyte interface. In this study, we establish transparent microelectrode arrays with high performance, great biocompatibility, and comprehensive in vivo validations from a recently developed, bilayer-nanomesh material composite, where a metal layer and a low-impedance faradaic interfacial layer are stacked reliably together in a same transparent nanomesh pattern. Specifically, flexible arrays from 32 bilayer-nanomesh microelectrodes demonstrated near-unity yield with high uniformity, excellent biocompatibility, and great compatibility with state-of-the-art wireless recording and real-time artifact rejection system. The electrodes are highly scalable, with 130 kilohms at 1 kHz at 20 μm in diameter, comparable to the performance of microelectrodes in nontransparent Michigan arrays. The highly transparent, bilayer-nanomesh microelectrode arrays allowed in vivo two-photon imaging of single neurons in layer 2/3 of the visual cortex of awake mice, along with high-fidelity, simultaneous electrical recordings of visual-evoked activity, both in the multi-unit activity band and at lower frequencies by measuring the visual-evoked potential in the time domain. Together, these advances reveal the great potential of transparent arrays from bilayer-nanomesh microelectrodes for a broad range of utility in neuroscience and medical practices.

INTRODUCTION

Mapping brain activities with high spatial and temporal precision is critical for fully understanding the cognitive functions of the human brain (*1*). Electrophysiology has been the gold standard to measure fast neuronal activities (*2*). While evolved from the original single wire/clamp to state-of-the-art microelectrode/clamp arrays, recording using electrodes intrinsically lacks the spatial resolution needed to reveal the sophisticated circuit wirings. In addition, pure electrophysiology is "blind" to cell types and the complicated dendrites and axons surrounding neurons, which are neural signal pathways (*3*). Optical recording and stimulation, among others, have established as complementary approaches to overcome these limitations (*2*, *4*). The synergism of combining the superior time resolution and signal-to-noise ratio (SNR) of electrophysiology with the exceptional spatial sampling and resolution of optical probing will enable us to connect the neuronal network function to the underlying molecular and cellular structures with unprecedented precision. Compelling examples of these synergisms include the localization of the functional inputs on a dendritic tree for constraining the rules for dendritic computations (*2*) and the role of single neurons in network dynamics (*5*). Yet, a dream experiment still remains to effectively combine electrical and optical approaches, at large scale and with great precision.

By making microelectrode arrays (MEAs) transparent, one can leverage the high temporal and spatial resolution advantages from both electrophysiology and imaging, respectively. High-performance MEAs also require densely packed microelectrodes with both high selectivity and sensitivity for recording neuron signals and/or modulating brain activities using electrical stimulation (*6*). For example, just microelectrode sites alone can already occupy up to 82% of the total array area in high-density, large-scale MEAs (*7*–*9*), blocking most of the field of view to look through them if they were not transparent. Modern MEAs have developed high-density, small–site area microelectrodes to achieve high selectivity (*10*). MEAs with electrode diameter down to 7 μm and electrode pitch down to 18 μm have been demonstrated to achieve cellular or subcellular resolution (*11*). An electrode of such small size is not only a necessity coming from the decreased pitch between them for high density but also a requirement to measure "single units," which are the electrophysiological signature of action potentials from single neurons (*12*). On the other hand, miniaturized microelectrodes also allow selective stimulation of a small and localized population of neurons (*13*). For many stimulation applications requiring a high density of microelectrodes packed in a small region, electrode diameter may not exceed 100 μm to achieve good specificity (*14*).

However, the need of small electrode size to achieve high selectivity poses major challenges to achieve good sensitivity, which demands sufficiently low electrochemical impedance from microelectrodes,

[1]Department of Electrical and Computer Engineering, Northeastern University, Boston, MA 02115, USA. [2]Center for Life Science, Boston Children's Hospital, Boston, MA 02115, USA. [3]Department of Bioengineering, University of California, Los Angeles, Los Angeles, CA 90095, USA. [4]School of Material Science and Engineering, Tsinghua University, Beijing 100084, China. [5]Department of Electrical and Computer Engineering, North Carolina State University, Raleigh, NC 27695, USA. [6]School of Optical and Electronic Information, Huazhong University of Science and Technology, Wuhan, Hubei 430074, China. [7]Department of Electrical and Computer Engineering, University of California, Los Angeles, Los Angeles, CA 90095, USA. [8]California NanoSystems Institute, University of California, Los Angeles, Los Angeles, CA 90095, USA. [9]Department of Bioengineering, Northeastern University, Boston, MA 02120, USA.
*These authors contributed equally to this work.
†Corresponding author. Email: h.fang@northeastern.edu (H.F.); michela.fagiolini@childrens.harvard.edu (M.F.)

because the electrode impedance is usually inversely proportional to its site area to a certain degree. Toward this end, modern MEAs have developed various low-impedance coatings on highly conductive metals and achieved low electrode impedance and high charge injection limit (*15*–*18*), guaranteeing neural recording with high fidelity and avoiding tissue damage during electrical stimulation. However, this trade-off will become a heavy burden in scaling previous transparent MEAs made of graphene (*3*, *19*) or indium tin oxide (ITO) (*20*–*22*) due to their limited conductivity and capacitive electrode/electrolyte interface, while most reliable low-impedance coatings are highly nontransparent. This dilemma between achieving selectivity and sensitivity has become a major concern for transparent MEAs.

Nanomeshed forms of conductors have emerged as an encouraging biocompatible material for future soft bioelectronics (*23*, *24*). Recently, we demonstrated an innovative bilayer-nanomesh approach by reliably stacking individual layers of metal and low-impedance coating—the exact materials used in modern MEAs—in the same nanomeshed pattern and achieved system-level high performance including microelectrode impedance, charge injection limit, and transparency (*25*). By template electroplating poly(3,4-ethylenedioxythiophene)-poly(styrenesulfonate) (PEDOT:PSS) (*17*, *26*) on gold (Au) nanomeshes, the final bilayer-nanomesh microelectrode has surpassed the performance of previous graphene and ITO microelectrodes by more than one order of magnitude in both impedance and charge injection limit, while with slightly less optical transparency. Here, we take a major leap forward by demonstrating flexible arrays of 32-channel bilayer-nanomesh microelectrodes with near-unity yield and high uniformity, along with their in vivo biocompatibility verification from histology studies and in vivo validations with concurrent calcium and two-photon imaging. The 32-channel bilayer-nanomesh arrays have demonstrated over 90% yield on average, with down to 10% impedance variation among all electrodes. Systematic bench characterizations using impedance spectroscopy, sine wave input, charge injection limit measurements, mechanical bending test, soaking test, and electrical stimulation test have successfully demonstrated the uniformity, robustness, and reliability of the bilayer-nanomesh MEAs. We also successfully achieved Au/PEDOT:PSS bilayer-nanomesh microelectrodes with site area down to ~314 μm^2 (that is, 20 μm in diameter), comparable to the size of a single neuron, while still possessing impedance of 130 kilohms at 1 kHz. This electrode performance is comparable to current nontransparent MEAs (*27*), such as the ones from Michigan probe. Meanwhile, the bilayer-nanomesh MEAs also achieved great compatibility with state-of-the-art ultra-wideband (UWB) links for wireless recording and real-time stimulation artifact cancelation, with demonstrations of rejecting 2 $V_{p\text{-}p}$ (peak-to-peak amplitude) interfering/artifact waveforms to precisely record 200-μV signals with errors ~20 μV, achieving a 100,000× signal/error ratio. Finally, in vivo electrophysiology recording with simultaneous two-photon imaging on the visual cortex of mice further validated the device functionality. The highly transparent 32-channel bilayer-nanomesh MEA allowed both wide-field epifluorescence and two-photon Ca^{++} imaging of visual cortex and surrounding areas with successful detection of visual-evoked potentials (VEPs) from multi-unit activity, while with no significant inflammation of the cortex due to the MEA implantation after 20 days. The results here establish the bilayer-nanomesh microelectrode approach as a practical pathway toward large-scale, high-density transparent arrays, with broad applicability in neuroscience and medical practices.

RESULTS

Transparent bilayer-nanomesh MEA fabrication

We fabricated the 32-channel Au/PEDOT:PSS nanomesh MEA on a flexible parylene C film, which serves as both transparent and minimally invasive substrate for the device. Figure 1A shows an actual device wrapped on a paper rod, exhibiting the excellent optical transparency and mechanical flexibility of the MEA. On top of the 10-μm-thick parylene C substrate, the microelectrodes consist of a nanomeshed bilayer of 25-nm-thick Au and a 85-nm-thick PEDOT:PSS, while the interconnects are exclusively from the Au nanomesh with a 4.5-μm-thick SU-8 layer as encapsulation. There is a 2-nm-thick chromium (Cr) layer between Au and the parylene C film for better adhesion, which is also in the shape of a nanomesh. Notably, we used SU-8 as the encapsulation material here only to facilitate via patterning. While SU-8 is being used in fabricating some biomedical devices, the long-term biocompatibility of SU-8 is still not well understood. It is important to note that our in vivo experiments with two-photon microscopy and long-term survival (up to 20 days) did not reveal any significant biocompatibility issues. For chronic recording and brain imaging, better encapsulating materials such as parylene C or PDMS (polydimethylsiloxane) are necessary. The schematic of the MEA is displayed in Fig. 1B, with a zoomed-in microelectrode image from the microscope shown on the left of Fig. 1C. The pitch between neighbored microelectrode sites is designed to be 400 μm, so that the 32-channel MEA can fit within a 3-mm-diameter circular surgery window. This level of electrode spacing is sufficient to capture the rich spatial information available and have been adopted for many previous studies (*6*, *28*, *29*). The scanning electron microscopy (SEM) image shown on the right of Fig. 1C provides more details about the Au/PEDOT:PSS bilayer-nanomesh structure, revealing a nearly perfect stacking of PEDOT:PSS coating on the Au nanomesh layer, with minimal to none PEDOT:PSS in the holes.

Figure 1D illustrates the detailed fabrication process of the Au/PEDOT:PSS nanomesh MEA. The fabrication starts with the deposition of polystyrene (PS) spheres (1 μm in diameter), which self-assemble at the air/water interface to form a monolayer and then transferred onto the parylene C substrate on a glass handle. After trimming the PS spheres with reactive ion etching (RIE), deposition and lift-off of Au generate an Au nanomesh layer. The nanomesh templates we used throughout this work have a width of ~70 nm and a pitch of 1 μm. After patterning Au nanomesh into the MEA, encapsulating the interconnects with a SU-8 layer, bilayer-nanomesh microelectrodes are achieved through template-electroplating PEDOT:PSS on the exposed Au nanomesh microelectrode sites in a mixture of ethylene dioxythiophene (EDOT) monomer and poly(styrene sulfonate) sodium salt (NaPSS) powder (with constant current 0.2 mA/cm^2 applied for 50 s, corresponding to a deposition rate of 1.7 nm/s) (*25*). Bilayer-nanomesh microelectrodes and nanomesh interconnects achieved from this process demonstrated transparency over a broad optical window (300 to 1100 nm), with over 70% transmittance at 550 nm, which is slightly lower compared to the graphene or ITO microelectrodes but still sufficient for optical measurements (fig. S1 B). We have successfully demonstrated bilayer-nanomesh MEAs with electrode diameter from 140, 80, 40, to 20 μm (fig. S2), and with typical 1-kHz impedance from 5.4, 12.1, 43.4, to 130.3 kilohms, respectively (Fig. 1E). To highlight the performance of Au/PEDOT:PSS nanomesh microelectrodes, we compared the impedances from bilayer-nanomesh microelectrodes to previously reported major transparent MEAs from graphene, ITO,

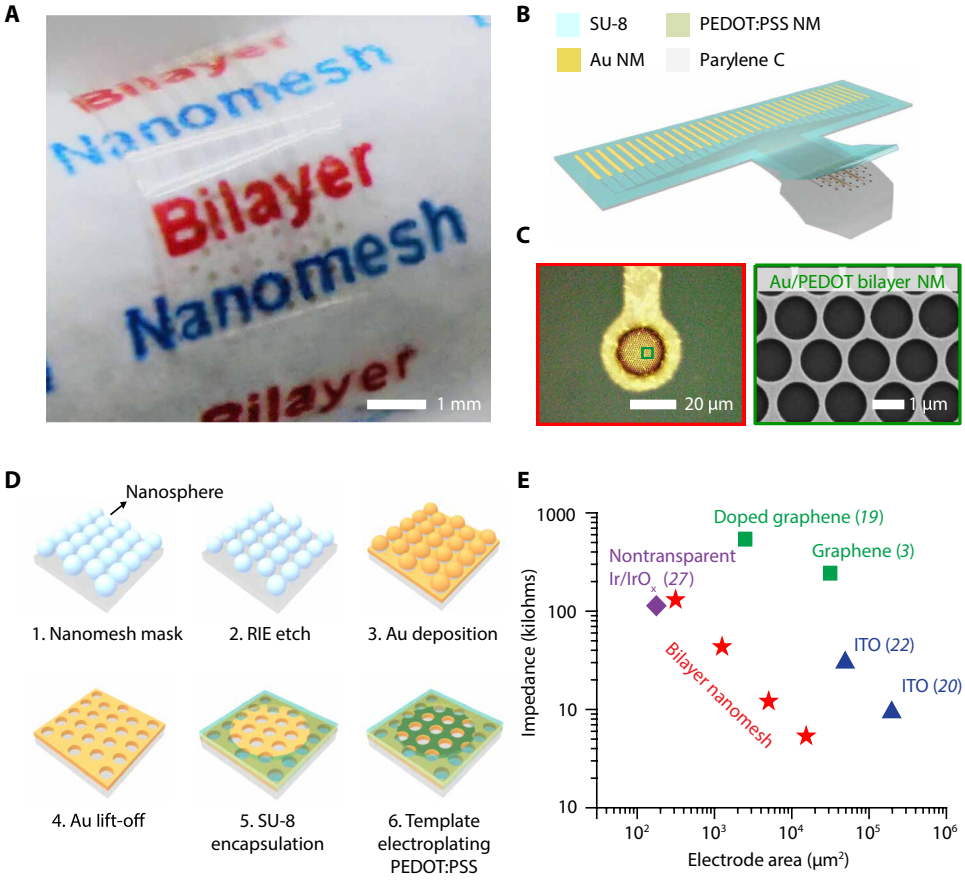

Fig. 1. Materials, fabrication strategies, and performance benchmarking of transparent, bilayer-nanomesh MEAs. (**A**) Photograph of a 32-channel Au/PEDOT:PSS nanomesh MEA wrapped on a paper rod. Scale bar, 1 mm. (**B**) Device schematic of the 32-channel Au/PEDOT:PSS nanomesh MEA in (A). (**C**) Left: Microscope image of a Au/PEDOT:PSS bilayer-nanomesh microelectrode (20 μm in diameter). Right: SEM image of a zoomed-in region of the microelectrode shown on the left. (**D**) Fabrication process of the bilayer-nanomesh MEAs. (**E**) Impedance of different bilayer-nanomesh microelectrodes versus electrode site area. Results from bilayer-nanomesh microelectrodes are benchmarked against the ones from major transparent MEAs from graphene, ITO, and nontransparent Michigan arrays. NM, nanomesh.

and state-of-the-art nontransparent ones (*3*, *19*–*22*, *27*, *30*). As expected, the Au/PEDOT:PSS nanomesh microelectrodes demonstrated 22× and 24× better impedance than the previous graphene (*19*) or ITO (*22*) ones of the same site area, while with slightly less transparency. Notably, at single-neuron size, the impedance of the transparent bilayer-nanomesh microelectrodes is comparable to the ones from nontransparent Michigan probes (*27*), highlighting the scalability of bilayer-nanomesh microelectrodes and the unique advantage from the bilayer-nanomesh approach. Spin coating of PEDOT:PSS layer on transparent ITO microelectrode is another solution for improving the scalability of transparent microelectrodes (*31*). However, the bilayer-nanomesh approach is unique and advantageous, especially for large-scale, flexible devices. First, the bilayer nanomesh used the exact same electrode materials in the state-of-the-art commercial MEAs (such as Michigan probes), but only to turn them transparent by nanomeshing, while delivering similar microelectrode performance (impedance, charge injection limit, etc.). This approach allows leveraging the existing knowledge and infrastructure from multidecade-long development and in vivo experience of these commercial MEAs. Second, a key vision for all transparent arrays is large-scale, high-density MEAs. In addition to microelectrode performance, another critical aspect is the interconnect. When fabricating large-scale, high-density devices, interconnects in the array will become long yet narrow. The interconnect line from Au nanomeshes has demonstrated much higher conductivity than the graphene and ITO ones (*3*), not limiting further scaling. Third, Au is ductile, which has much better mechanical properties than ITO for ultraflexible or even future stretchable devices. On the other hand, the fabrication of Au nanomesh is much easier than that of graphene, especially at the large scale. Last, more reliable PEDOT:PSS coating develops from electroplating (*14*), which will render the layer highly nontransparent. Making PEDOT:PSS into nanomesh therefore is a transformative way to allow light to transmit through it.

Bench testing of 32-channel bilayer-nanomesh MEAs

We have successfully achieved 32-channel Au/PEDOT:PSS nanomesh MEAs from in-house fabrication with an average yield over 90% and great uniformity (fig. S3). Figure 2 (A and B) shows the electrochemical impedance spectroscopy (EIS) response (measured with frequencies ranging from 1 Hz to 1 MHz) and the 1-kHz impedance histogram from 31 working (defined by impedance) microelectrodes (80-μm diameter) in one 32-channel array, revealing uniform microelectrode performance with an average impedance of 12.1 ± 1.2 kilohms. The inset of Fig. 2B shows the spatial distribution of microelectrode impedance in the array, from which one can visually observe the high uniformity of the array performance. Such low impedance and great uniformity are critical for large-scale, high-fidelity

neural recordings, since thermal noise usually increases with electrode impedance directly. To demonstrate high-fidelity signal recording due to low impedance, we conducted a bench recording test by immersing the Au/PEDOT:PSS MEA into phosphate-buffered saline (PBS) solution with the application of a 1000 Hz, 316 $\mu V_{p\text{-}p}$ (peak-to-peak amplitude) sine wave signal to the PBS solution through a platinum wire electrode. This high fidelity further validates the significant noise reduction from Au/PEDOT:PSS nanomesh microelectrodes compared to that from Au nanomesh microelectrodes observed in our previous work (*25*). Figure 2 (C and D) displays the recorded sine wave waveform and its power spectra density, after a 0.1- to 5000-Hz bandpass filter and notch filters to remove the 60 Hz (power line frequency) and its harmonics. The bilayer-nanomesh MEAs were able to record signals with high fidelity with a high SNR and uniformity shown in Fig. 2E. Distribution curve of the SNR histogram shows an average SNR of 32.78 ± 0.32 dB, corresponding to a 2.62-μV root mean square (RMS) noise, which will provide minimal noise interference during neural recordings. More bench recordings with sine wave inputs at different frequencies are available in fig. S4.

Another important parameter for microelectrode performance is its charge injection limit. Electrical stimulation is typically implemented

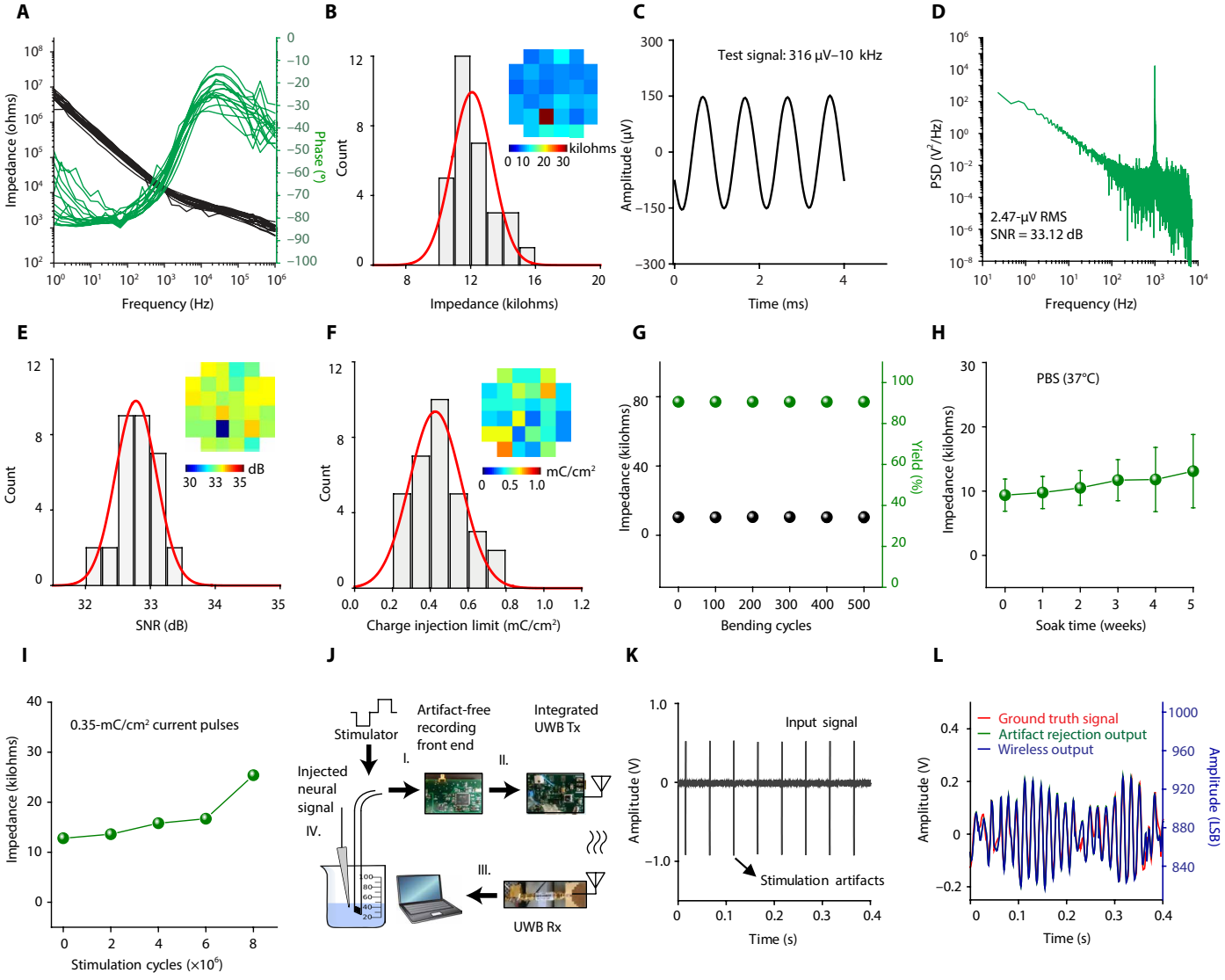

Fig. 2. Bench testing of 32-channel bilayer-nanomesh MEAs. (**A**) Impedance magnitude and phase spectra of the 31 working electrodes in a 32-channel Au/PEDOT:PSS bilayer-nanomesh MEA. (**B**) Electrode impedance histogram of the 32-channel Au/PEDOT:PSS nanomesh MEA in (A). Inset: Impedance colormap with respect to actual channel position. (**C**) Bench recording output of a 1000-Hz, 316 $V_{p\text{-}p}$ sine wave input using the Au/PEDOT:PSS nanomesh MEA in (A). (**D**) Power spectra density of recorded sine wave output in (C). (**E**) SNR histogram from all electrodes with the bench recording in (C). Inset: SNR colormap with respect to actual channel position. (**F**) Histogram of charge injection limit of all electrodes from the 32-channel Au/PEDOT:PSS nanomesh MEA in (A). Inset: Charge injection limit color map with respect to actual channel position. (**G**) Average electrode impedance and array yield as a function of bending cycles with a bending radius of 4 mm. (**H**) Average electrode impedance as a function of weeks after soaking for devices immersed in PBS (pH 7.4) under 37°C. (**I**) Electrode impedance as a function of stimulating cycles with current pulses (0.35 mC/cm^2). (**J**) Schematic of the experimental setup of the wireless recording with stimulation artifact rejection with the 32-channel Au/PEDOT:PSS nanomesh MEA. (**K**) Input neural signal contaminated with large stimulation artifacts. (**L**) Ground truth neural signal overlapped with artifact rejection output (left *y* axis) and wireless output (right *y* axis) for comparison. PSD, power spectra density; Tx, transmitter; Rx, receiver; LSB, least significant bit.

by applying cathodic first, biphasic current pulse with duration less than 0.5 ms to microelectrodes (*32*). The polarization of microelectrodes under current bias should not exceed the water window (−0.6 to 0.8 V) to prevent water from hydrolyzing, which will generate unwanted by-products and also cause damage to electrodes and surrounding tissues. We characterized the charge injection limit of Au/PEDOT:PSS nanomesh MEA, at which the voltage transient of microelectrodes reaches the water window. Figure 2F shows the histogram and spatial distribution of charge injection limit of one 32-channel Au/PEDOT:PSS nanomesh MEA. With 85-nm-thick PEDOT:PSS, the average charge injection limit of the MEA is 0.43 ± 0.14 mC/cm^2, consistent with our previous characterization of single Au/PEDOT:PSS nanomesh microelectrode (*25*). We also expect that the charge injection limit will increase with more PEDOT:PSS coating, if less transparency is tolerable. For example, with 255-nm-thick PEDOT:PSS in the bilayer nanomesh, the charge injection limit can increase to 1 mC/cm^2, which is suitable for most high-density microstimulations with good site specificity (*33*). Detailed information about the method to measure charge injection limit is available in Materials and Methods. Herein, we have successfully achieved the 32-channel Au/PEDOT:PSS nanomesh MEA with both high yield and uniformity for the first time. Meanwhile, the bilayer-nanomesh microelectrode is capable of scaling down to an area of ~314 μm^2 with ~130-kilohm impedance at 1 kHz. This electrode performance is comparable to state-of-the-art Michigan MEAs. Together, these two demonstrations paved the way for future large-scale, high-density arrays from the bilayer-nanomesh microelectrode approach.

Strong mechanical and electrochemical robustness of neural-electrode array is essential for in vivo measurements and neural recording and/or stimulation after implantation. We demonstrated excellent flexibility of our bilayer-nanomesh MEA by bending the array with a radius of 4 mm for up to 500 cycles. No significant yield or impedance change was observed, as is shown in Fig. 2G. Soaking test was performed under physiological temperature (37°C) for up to 5 weeks in PBS solution (pH 7.4). The impedance remained nearly the same as soaking (Fig. 2H), and no layer delamination was observed from microscope examination. Stimulation test was conducted via applying continuous cyclic submillisecond current pulses (0.35 mC/cm^2) to the MEA in PBS solution. As shown from Fig. 2I, the impedance of bilayer-nanomesh microelectrode was stable up to stimulation of 6 million pulses (about 36 hours continuously), demonstrating clinically relevant reliability (*34*). Over 10 million pulses of stimulation may lead to a significant impedance increase due to eventual delamination of the PEDOT:PSS layer, consistent with previously reported PEDOT:PSS electrodes from electrodeposition (*14*). Light-induced artifacts of Au/PEDOT:PSS nanomesh MEA array have also been studied using light sources with two different wavelengths (470 and 590 nm), and the results (fig. S5) are in good agreement with previous work (*25*). We note that these artifacts only emerge at large illumination intensity (>10-μV RMS when above ~2.1 mW/mm^2 for 470-nm excitations with a roughly linear decay); therefore, it is not an issue for regular optical imaging, such as calcium imaging, which requires only an average of 0.28 mW/mm^2 imaging power. High-power optogenetic experiments should use advanced on-line signal processing unit and/or microfibers to avoid direct illumination on the electrodes to minimize artifacts. Here, we further demonstrate an artifact-free, transparent ITO/PEDOT:PSS bilayer-nanomesh microelectrode to fulfill the requirement of high-power optogenetics applications. The thicknesses of ITO and PEDOT:PSS are 60 and 85 nm, respectively. There is also a 1-nm-thick Cr adhesion layer between the ITO and the substrate. The use of the similar fabrication process demonstrated that ITO/PEDOT:PSS nanomesh microelectrodes (80-μm diameter) have an average transmittance over 80% and impedance down to 65 kilohms (fig. S6). The results show that our bilayer-nanomesh approach can be successfully translated to other materials, and, in this case, the ones not susceptible to photon-induced artifacts.

To demonstrate application of the 32-channel bilayer-nanomesh MEA as a bidirectional neural interface, we have used a custom-designed neural stimulator, recording, and wireless communication electronics to conduct simultaneous stimulation and recording. The recording is inherently challenging in dense microelectrodes, as injection of stimulus current into these microelectrodes generates a large amount of stimulation artifact that easily overwhelms a standard recording amplifier, causing irrecoverable signal loss. This signal loss is prevented in our custom electronic design by use of a unique circuit topology that rejects the large artifact online and continuously records the underlying neural signal. In addition, the neural signals are wirelessly transmitted during recording through our UWB wireless design, which is capable of supporting large numbers of recording channels simultaneously.

We have conducted bench testing of concurrent wireless recording and stimulation with the 32-channel transparent bilayer-nanomesh MEA by using our custom neural stimulator (*35*), custom artifact rejection–capable amplifiers (*36*), and UWB transmitter circuitry (*37*), as briefly illustrated in Fig. 2J. A detailed photograph of the entire experimental setup is available in fig. S7. A stimulus signal was injected into the nanomesh MEA, which was immersed into a standard saline solution. The saline solution also contained a wire electrode which was connected to a signal generator preprogrammed with an emulated neural signal. The neural signal was a prerecorded electrocorticography (ECoG) signal segment from a human patient at the onset of a seizure. The electrode channel used for stimulation was simultaneously connected to the artifact rejection amplifier circuit, which recorded both the artifact waveform with amplitude ~2 $V_{p\text{-}p}$ (Fig. 2K) and the neural signal with amplitude <200 μV. The amplifier's analog and digital circuits learned and rejected the artifact, revealing only the underlying neural signals at its output. The output was digitized and further wirelessly transmitted by the UWB circuits. A UWB receiver located 50 cm away from the transmitter received and demodulated the signal stream, which is then captured by the data acquisition device for observation. The observed received signal is compared to the ground truth neural signal and shows highly close resemblance (Fig. 2L) despite the contamination by large artifacts at the input. Specifically, the resulting output signal error with respect to the ground truth is <20 μV, yielding artifact rejection ratio of 100,000× or 100 dB. We also performed the same test with pure Au nanomesh microelectrodes. Because of a significantly lower charge capacity of the microelectrode and a larger electrode impedance, the stimulation current was lowered while keeping other conditions the same. This compromise allowed for stimulating within the water window and avoiding irreversible reactions at the microelectrode interface while performing artifact rejection. The resulting output signals (fig. S8) are very similar to those of the Au/PEDOT:PSS microelectrode. The similarity is due to the fact that the artifact rejection system is largely not specific to the electrode characteristics or the current injected, but rather records and rejects the voltage waveform of the resulting artifact. This first-time demonstration of high-fidelity wireless recording from transparent bilayer-nanomesh microelectrodes with real-time stimulation

artifact cancelation will enable concurrent wireless electrical recording and stimulation as well as optical modalities in future physiological experiments. A multichannel version of the wireless online artifact rejection system is currently in progress and will be integrated with large-throughput nanomesh MEAs as a compatible head stage for electrophysiology recording and stimulation in future work.

In vivo implant and histology studies of Au/PEDOT:PSS nanomesh MEAs

The 32-channel transparent bilayer-nanomesh MEAs of different electrode diameters have been implanted and tested on the surface of the brain of an adult mouse. At the postnatal day P60 (60 days after birth), a mouse was deeply anesthetized using isofluorane and underwent a surgery procedure in which both the bilayer-nanomesh MEA and a cranial window have been implanted, followed by recovery and habituation for head restraint and by recording/calcium (Ca^{++}) imaging after 20 days (Fig. 3A). The surgery consisted of the implantation of a headbar for head restraint on the skull (Fig. 3B), by a 3-mm craniotomy and durotomy on the right side of the brain. The dura is a light scattering tissue, and its removal was necessary for a good quality of the Ca^{++} imaging (*38*, *39*). Then, an adeno-associated virus (AAV) expressing the fluorescent Ca^{++} indicator GCaMP6s in neurons (AAV9.Syn.GCaMP6s.wpre.sv40 from Penn Vector Core) was injected in four different sites surrounding the visual cortex (300 nl per injection) at a depth of about 400 μm (procedure not shown). The virus infected the visual cortex in about 2 weeks, allowing the expression of the fluorescent protein GCaMP6s, whose fluorescence is Ca^{++}-dependent and is a good indicator of neuronal activity (*40*). After the virus injection, the transparent MEA was laid on the surface of the visual cortex (Fig. 3C) and covered with a glass window (Fig. 3D). The glass window was sealed to the skull with cyanoacrylate (Vetbond, 3M), and all exposed areas of the skull around the window and around the headbar have been sealed with dental cement mixed with black dye (to decrease the light contamination coming from ambient illumination during Ca^{++} imaging). The anisotropic conductive film (ACF) cable connecting the array was wrapped on the headbar after the surgery and during the recovery of the mouse. After the recovery, the mouse was habituated every other day to be head-restrained on the styrofoam ball, and finally it was recorded and imaged 20 days after the surgery.

We performed an ex vivo staining of both the implanted cortex and the not implanted one for the ionized calcium-binding adapter molecule 1 (IBA1), which is a marker for microglia activation and allows us to measure the inflammatory response. The staining was performed 20 days after the surgery. The IBA1 staining has shown no significant inflammation of the cortex due to the electrode implantation (Fig. 3, E and F). The left cortex (nonimplanted) was stained as control reference. We also stained the brain of a mouse implanted with both the transparent MEA and the cranial window implantation, observing only the cortical compression due to the cranial window implant, but not the microglia activation (fig. S9), indicating that the bilayer-nanomesh MEAs are fully biocompatible.

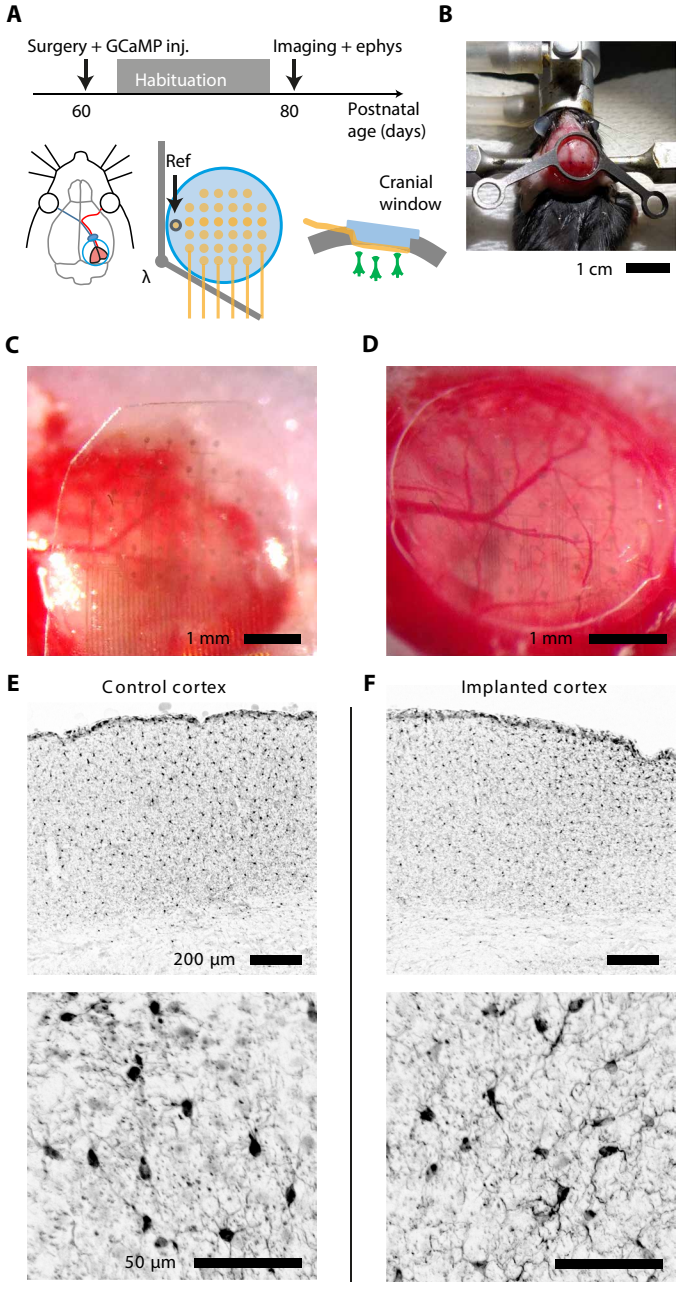

Fig. 3. Surgery procedure and in vivo histology studies of bilayer-nanomesh MEAs. (**A**) Schemes of the sequence of the experiments, the positions of the MEA and the cranial window on the mouse brain. (**B**) Installation of the headbar. (**C**) Implantation of the transparent MEA on the brain. (**D**) Enclosure of the transparent MEA with the cranial window. (**E** and **F**) IBA1 staining for evaluating possible microglia activation on the control cortex (E) and on the cortex implanted only with the transparent MEA (F).

Concurrent electrophysiology with two-photon imaging

Twenty days after the surgery, at the postnatal age P80, the mouse had fully recovered, and the expression of the GCaMP6s protein was sufficient to acquire two-photon Ca^{++} imaging and epifluorescence imaging on the visual cortex. The mouse was head-restrained on a floating styrofoam ball, but was free to move (Fig. 4A). The ACF cable was connected to the recording system (Intan RHD2000 board, RHD2132 headstage). A custom-made pupillometer was focused on the eye of the mouse to track arousal changes. Pupil diameter is a good proxy for general arousal of the mouse, which in turn controls cortical gain (*41*, *42*). As proof of concept, a 32-channel epicortical MEA of 80-μm bilayer-nanomesh microelectrodes allowed both wide-field epifluorescence of the visual cortex and the surrounding areas (Fig. 4B and movie S1) and two-photon Ca^{++} imaging (Fig. 4C

and movie S2). The fluorescence from the brain area covered by the electrode is 73 ± 3% compared to the one from the area immediately surrounding the electrode (fig. S10). This ratio is the product of both the transmission in excitation from the epifluorescence lamp (350 to 450 nm) and in emission from the GCaMP6s fluorescence (500 to 550 nm). This high ratio indicates a high transparency of the electrodes on both the two wavelength bands, consistent with our previous bench testing, making them suitable for in vivo imaging. The microelectrodes have allowed for high transparency and image quality both in epifluorescence Ca^{++} imaging [conventional one-photon

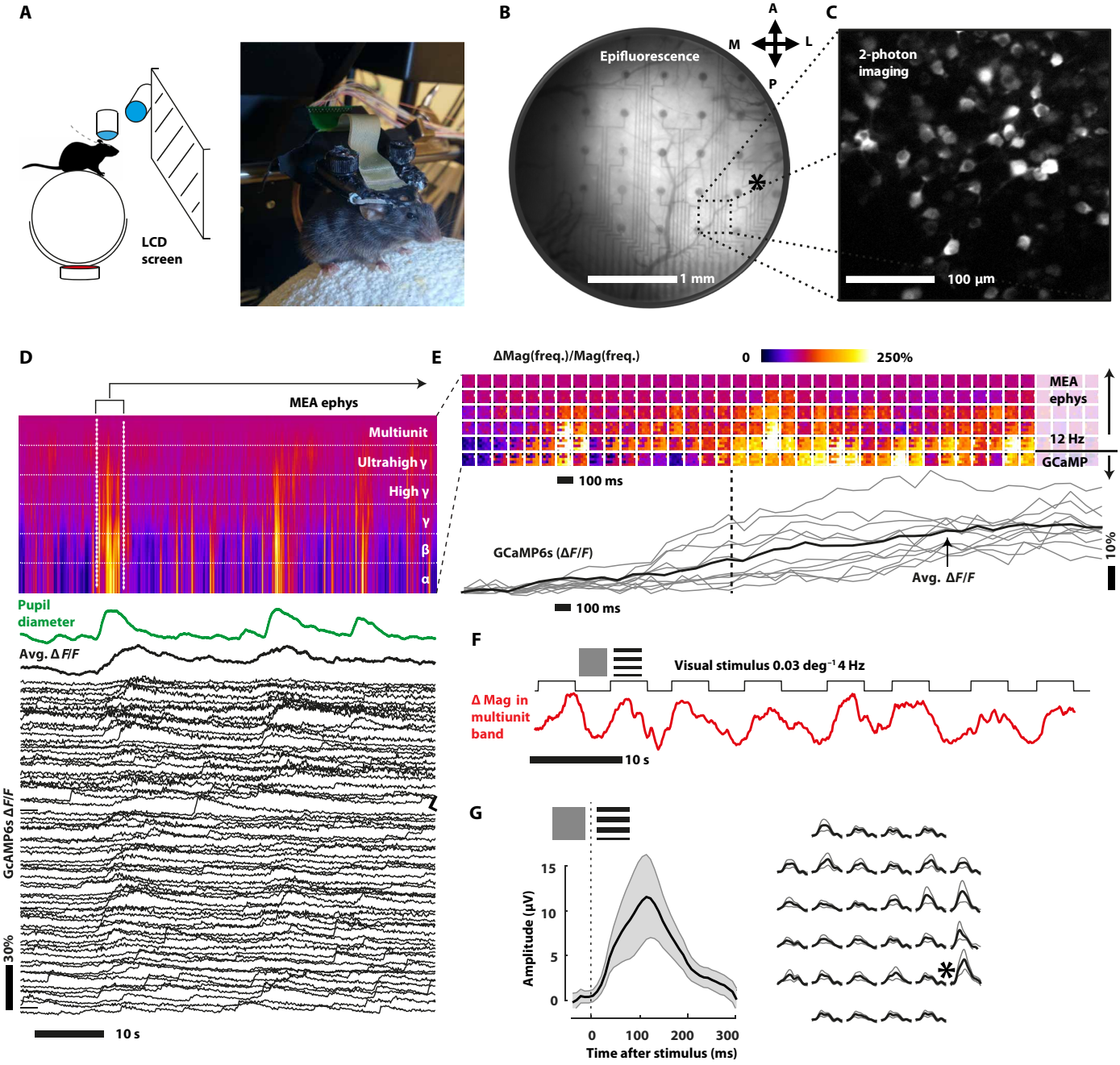

Fig. 4. Simultaneous two-photon Ca^{++} imaging and electrophysiological recording from a bilayer-nanomesh MEA on the brain of an awake mouse. (**A**) Head-restrained awake mouse on a floating styrofoam ball, watching visual stimuli. (**B**) Wide-field epifluorescence of the visual cortex and the surrounding areas. The asterisk indicates the binocular area of the visual cortex. (**C**) Temporal autocorrelation from a two-photon imaging movie (1-s lag), indicating neurons expressing the Ca^{++} indicator GCaMP6s. (**D**) Simultaneous electrophysiology recording (spectrogram, top), arousal (pupil diameter, middle), and two-photon imaging (Δ*F*/*F* traces representing single-neuron Ca^{++} activity (bottom). (**E**) Magnification of the spectrogram and Ca^{++} traces during the onset of a spontaneously induced high arousal event. Each square contains the increase in magnitude of the 32-channel electrophysiology signal in a specific frequency band (from top to bottom: α, β, γ, high γ, ultrahigh γ, and multi-unit). The dashed line is a guide to the eyes to show when the average GCaMP expression is rising (the line corresponds to the 50% of the maximum Δ*F*/*F*). (**F**) Modulation of the power in the high-frequency band (average on all 32 channels) during the alternation of visual stimuli and gray screen. (**G**) Visual-evoked response in the time domain (lower frequency). The asterisk indicates the position of the binocular area of the visual cortex. LCD, liquid crystal display.

imaging, with conventional fluorescein isothiocyanate (FITC) filters] and in two-photon excitation Ca^{++} microscopy (930-nm pulsed excitation, 500- to 550-nm emission filter). Although the region underneath microelectrodes is darker than the surrounding areas, a single neuron can still be clearly observed and imaged. The high quality was confirmed even on the dendrites in layer 1 (depth <50 μm), where most of the imaged area is covered by the transparent microelectrodes (80-μm diameter) (fig. S11). The high transparency of these electrodes is strongly necessary for two-photon imaging, since the two-photon excitation process scales with the square of the excitation power, and the light from the fluorescence has to travel across electrodes again on its way back to the detector. Hence, the high transparency of the electrodes allowed a good spatial resolution and a good SNR of the fluorescence, as it is clearly shown in the raw data of movie S2 and in the 1-s lag temporal correlation image of this movie (Fig. 4C). To evaluate possible changes of impedance after implanting onto the brain, we recorded over a period of 2 weeks at regular interval starting 1 day after implantation (fig. S12). The values were compared to the one collected at the bench testing session (fig. S10). An increase of impedance magnitude at 1 kHz by about 30 kilohms was observed after the first day of implantation. This increase is consistent with existing literature (*10*), presumably due to the fact that our bilayer-nanomesh electrodes are using the very same materials as in the commercial electrodes such as Michigan arrays. Notably, the impedance was remarkably stable over the course of the 2-week recordings. Figure 4D shows an in vivo electrophysiology recorded simultaneously with two-photon Ca^{++} imaging on an awake mouse. During the recording, a monitor showed visual stimuli to the mouse [moving sinusoidal gratings, spatial frequency (SF) = 0.03 deg^{-1}; temporal frequency (TF) = 4 Hz, 4 s, 100% contrast]. Electrophysiology, single-neuron calcium (Ca^{++}) transients, and pupillometry were acquired. The latter was used as a measure of the general arousal of the mouse during the session. As Fig. 4D shows, on the 10-s timescale, both the electrophysiology activity and the single-neuron Ca^{++} traces are modulated by the arousal (pupil diameter). The correlated response of electrophysiology, Ca^{++} imaging, and arousal during the whole recording can also be seen in movies S3 (30× faster than the real time) and S4 (3× faster than the real time). As Fig. 4D shows, when the pupil becomes bigger and the mouse is more aroused, the MEA is promptly measuring an increase in activity from α to ultrahigh γ (8 to 300 Hz). The transparent MEA is highly sensitive to detect these arousal changes in the cortical state.

The onset of a spontaneously induced high arousal event is magnified in Fig. 4E. Each square contains the increase in magnitude of the 32-channel electrophysiology signal in a specific frequency band (from top to bottom: α, β, γ, high γ, ultrahigh γ, and multi-unit) and spaced by 100 ms between squares. The lower panel of Fig. 4E shows the average ensemble response of the Ca^{++} indicator GCaMP6s. While the lower frequency of the spectrogram (α band, 8 to 12 Hz) contains essentially the same temporal information of GCaMP imaging (which has an activation time around 100 ms), the higher frequencies contain the information on much faster events that otherwise could not be resolved using actual Ca^{++} probes, highlighting the benefit from the concurrent measurements. For example, by measuring the power in the multi-unit band (300 to 7000 Hz, temporal window for Fourier transform 100 ms) which arises directly from neuronal action potentials, we observed a clear correlation of multi-unit activity with the onset and the duration of the visual stimulation (Fig. 4F). As it can be clearly seen, these electrodes are indeed able to measure multi-unit activity arising from evoked response. The average among all electrodes is shown in Fig. 4F, while the map of single electrode responses can be observed in movie S5 (3× faster than the recording) in which evoked cortical activity (higher, color-coded in red) and spontaneous cortical activity (lower, color-coded in green) are alternated on the basis of the stimulus/nonstimulus presentation. The sensitivity in the 300-Hz to 7-kHz band is fundamental for measuring spikes from single neurons, which carry in their temporal information important aspects of cortical processing. Because of their low impedance, these electrodes are good candidates for single-unit detection in future experiments, once the electrodes are implanted intracortical with close proximity to the neurons. To address the specificity of the epicortical electrodes, we recorded the response to visual stimuli and measured the average evoked response potential in the time domain. This standardized response, which is typically higher in the layer 4 of the visual cortex (at about 400-μm depth from the surface), can be still observed on the surface of the brain (layer 1) (*43*). Figure 4G shows the VEP response to the stimulus from one strongly activated area of the visual cortex. Data were collected from one electrode and averaged. This procedure was repeated for all the other electrodes. A map of the response (right panel of Fig. 4G) shows a localized response very close to the maximum of the expected visual response for a binocular stimulation (0.5 to 1.0 mm anterior from lambda, 2.7 to 3.2 mm lateral from midline; see asterisk in Fig. 4B), corresponding to the more lateral microelectrodes on the right (see asterisk in Fig. 4G). As it can be clearly seen, only the right area is activated, which is the one correspondent to the binocular visual cortex. Notably, the results achieved from this work are the first-time in vivo validations of the Au/PEDOT:PSS bilayer-nanomesh MEA. We have proved its biocompatibility and also the capability of our device to distinguish the response from different areas of the brain based on their cortical functions, both from the electrophysiology recording and two-photon imaging approaches. This full biocompatibility is essential for the future implant of bilayer nanomesh or any nanomesh-based MEAs. The ability of two-photon imaging through nanomesh microelectrodes and interconnects critically validates the designed utility of the bilayer-nanomesh MEAs. We see no fundamental hurdles in deploying future large-scale, high-density bilayer-nanomesh MEAs in vivo.

DISCUSSION

In summary, here we present materials strategies, integration schemes, and in vivo protocols that establish the use of Au/PEDOT:PSS bilayer-nanomesh microelectrodes as high-performance transparent arrays. Because of the superior electrochemical performance including low impedance and high charge injection limit, we achieved single-neuron–sized microelectrodes with low impedance, beneficial for high-fidelity, highly specific neural recording and selective stimulation. Systematic bench characterizations revealed that flexible arrays made of these bilayer-nanomesh microelectrodes could achieve high uniformity, reliability, and great compatibility with state-of-the-art wireless recording artifact-rejecting electronics. In vivo validations of bilayer-nanomesh MEAs demonstrated that they are biocompatible and are fully compatible with two-photon Ca^{++} and epifluorescence imaging with successful epicortical recording in awake mice and at across all the frequency bands relevant for describing brain activity. In particular, multi-unit activity and low-frequency VEP were

detected at a high spatial resolution. The millisecond regime is especially important in cortical processing, since neuronal spikes occur in this time regime, and since both time and delayed correlations in activity among different neurons can encode interesting network properties. Detecting these fast neuronal activities is critical for understanding neural processing. From the neuroscience perspective, transparent MEAs are the ideal bridge between the spatial precision of single neuron Ca^{++} imaging and the temporal precision of single-electrode electrophysiology.

By adding two-dimensional spatial information to the excellent time resolution of MEAs, we will have the proper tool to reveal which traveling waves characterize cortical rhythms in the brain. Both high electrode density and transparency are necessary in the future for understanding the origin of the signals measured in electroencephalography, ECoG, and even field and action potentials. Also, by measuring simultaneously electrophysiology and imaging, we will be able to understand what cellular activity hides below those brain rhythms which characterize cortical states in both mice and humans. Hence, the development of high-performance, transparent Au/PEDOT:PSS bilayer-nanomesh MEA would undoubtedly facilitate the advancement of brain mapping. Further efforts include developing large-scale, high-density MEAs using bilayer-nanomesh materials for in vivo brain recording with simultaneous optical imaging and optogenetics interventions. While only epicortical recordings were conducted here, it is also amenable in the near future to developing penetrating bilayer-nanomesh MEAs with appropriate insertion aids for spatially resolved intracortical single-unit detection.

MATERIALS AND METHODS

Materials and tools

Polystyrene nanospheres (carboxyl latex bead, 4% w/v, 1.0 μm) and polyethylene oxide (PEO) were purchased from Thermo Fisher Scientific. EDOT monomer and NaPSS powder were purchased from Sigma-Aldrich. All materials were used as received. SEM (Supra 25 SEM) was used to characterize the structure of Au or Au/PEDOT:PSS bilayer nanomesh. Gamry Reference 600+ potentiostat/galvanostat/ZRA was used for electrodeposition and EIS. Intan stimulation/recording system (Intan Technologies) was used for impedance measurement at 1 kHz, bench signal recording, and charge injection limit characterization. A dual light-emitting diode (LED) LEDC2 (Doric Lenses Inc.) was used for light-induced artifact characterization.

Fabrication of Au nanomesh

The fabrication of the Au nanomesh began with the air-water interface technique for the deposition of PS nanospheres on a prepared flexible substrate. PEO was added to the PS solution to improve the close packing of nanospheres and reduce multilayer area (fig. S13). Detailed process is shown in our previous publication (*25*). Then, inductively coupled plasma RIE trimmed down the size of PS spheres. The etching conditions were 40 sccm (standard cubic centimeter per minute) of O_2, 2 sccm of CHF_3 (fluoroform), 25 mT, 100 W for radio frequency power (RF_1), 150 W for RF_2, and 45 s. E-beam evaporation deposited 2 nm of Cr and 25 nm of Au using 0.5 and 1 A/s rate, respectively. Lift-off in chloroform for 1 min finalized the fabrication process, generating Au nanomesh structure.

Fabrication of Au nanomesh microelectrodes

The process began with spin-coating positive photoresist (S1813, Shipley) on the fabricated Au nanomesh using 3000 rpm for 30 s. Then, optical photolithography defined the MEA with ultraviolet (UV) exposure and development. Wet etching with gold and chromium etchants yielded the final shape of the array. Acetone, isopropyl alcohol (IPA), and deionized (DI) water rinse removed the remaining photoresist. Then, encapsulation of the electrode began with spin-coating SU-8 2005 using 3000 rpm for 30 s to define sensing area. After soft baking at 65°C for 1 min and 95°C for 3 min, UV exposed the SU-8 for 6.5 s, followed by the same two-step baking recipe for postexposure baking. Then, sonication for 5 s in SU-8 developer and rinsing with fresh SU-8 developer and IPA finalized the SU-8 patterning. Hard bake at 200°C for 20 min completely cured the SU-8 layer.

Electrodeposition of PEDOT:PSS

We first performed treatment using UV/ozone (Bioforce Nanosciences Inc., Procleaner 110) for 20 min to remove organic residue from the MEA surface. PEDOT:PSS was then electrodeposited on the Au nanomesh template by electropolymerization of a mixture of EDOT monomer and NaPSS powder. NaPSS powder (0.1 mol/liter) was added into 150 ml of DI water and stirred for 20 min. Then, EDOT (0.01 mol/liter) monomer was added and stirred for another 30 min before use. The solution was then used for electroplating with typical three-electrode configuration. An Ag/AgCl electrode was used as reference electrode, and a platinum wire was used as counter electrode. Eventually, we applied current density (0.2 mA/cm^2) to the Au nanomesh microelectrodes in the prepared solution for 50 s, forming the PEDOT:PSS nanomesh layer.

Electrochemical impedance spectroscopy

Microelectrode impedance magnitude and phase spectra were measured using Gamry Reference 600+ Potentiostat/Galvanostat/ZRA (Gamry Instruments Inc). We swept frequencies from 1 Hz to 1 MHz with an alternating current measuring voltage of 10 mV. A three-electrode configuration was also adopted here with Ag/AgCl reference electrode and platinum wire as counter electrode, both immersed in 0.01 M PBS solution. We measured impedance at 1 kHz from the Intan Stimulation/Recording System (Intan Technologies) to confirm the results. The data used in Fig. 2A were measured from the Intan system, with one microelectrode in the array as reference electrode.

Methods

Animals

All procedures were approved by the Institutional Animal Care and Use Committee at Boston Children's Hospital. We used C57BL6 adult male mice.

Bench recording test

Bench recording test was conducted using sine wave signal generated from a function generator. The amplitude of input signal was 316 $V_{p\text{-}p}$ after a 50-dB attenuator, and the frequencies changed from 100 to 1000 Hz. The MEA was bonded to a customized printed circuit board (PCB) through an ACF cable, and then connected to the data acquisition system. We collected real-time data with an online 60-Hz notch filter using the Intan Stimulation/Recording System. Another 0.1- to 5000-Hz bandpass filter was applied after data acquisition using MATLAB R2016a software. MATLAB software also enabled the noise analysis including SNR and RMS noise calculation in this work.

Charge injection limit characterization

We conducted voltage excursion measurement to derive charge injection limit of Au/PEDOT:PSS nanomesh MEA. A three-electrode configuration was used in a standard PBS solution (pH 7.4) with Ag/AgCl reference electrode and Pt counter electrode. Intan RHS2116 microchip (Intan Technologies) provided the customized biphasic current pulses to stimulate the single microelectrodes. We connected all electrodes to the microchip correspondingly. Then, we connected the microchip to the Intan stimulation/recording controller (Intan Technologies), which was connected and controlled by computer software. We gradually increased the amplitude of the current until either the most positive voltage (E_{ma}) reached +0.8 V or the most negative voltage (E_{mc}) of microelectrodes reached −0.6 V, and then calculated the maximum charge injection without exceeding the water window. Access voltage (V_a), which illustrates the voltage drop resulting from ionic conductivity of electrolyte, was considered when we defined E_{ma} and E_{mc}. V_a can be estimated from either the onset or the end of a current pulse. A common strategy to define V_a is to add a short interphase period (here, it is 66.7 ms) between two continuous pulses. The highest (lowest) voltage minus (plus) V_a gives E_{ma} (E_{mc}). In this case, we used cathodic first, symmetric, charge-balanced biphasic current pulse with 500-ms width and 66.7-ms interphase for the charge injection limit characterization. We also applied 0.2 to 0.6 V positive bias to the microelectrodes versus the Ag/AgCl reference microelectrode to derive the maximum charge injection limit. Positive biases were delivered to the microelectrodes through direct current power supply across a 10-megohm resistor.

Light-induced artifacts characterization

Dual LED LEDC2 (Doric Lenses Inc.), which was connected to Doric fibers, provided light with two different wavelengths (470 nm, blue; 590 nm, amber) for light-induced artifact characterization. Driving current of the LED ranges from 0 to 1000 mA. The tip of the fiber was attached in the center of 32-channel MEA surface. The Intan Stimulation/Recording System recorded the artifact peaks with bandpass filter from 0.1 to 10,000 Hz and a 60-Hz notch filter.

Surgery

For both imaging and electrophysiology, both cranial window and the transparent 32-channel MEA were installed on the brain of the mouse. The mouse was anesthetized using isoflurane and was transferred to a stereotaxic frame, and an approximate 1-cm^2 skin flap was removed from the skull using sterile scissors. A drop of 1% lidocaine + epinephrine was applied to the exposed skull and overlying muscle to reduce pain and avoid bleeding. The skull was then scraped with a spatula to produce a clean surface for subsequent adhesion. A titanium head bar was glued to the skull using cyanoacrylate (Vetbond, 3M). Then, an area of the skull with 4-mm diameter was carefully thinned with a drill bit, and then lifted away using forceps. The dura was removed using forceps. Then, an AAV9.Syn.GCaMP6s.wpre.sv40 virus was injected on the brain in four different locations around the visual cortex. Every injection consisted of 300 nl at a depth of approximately 400 μm. Then, the electrode was gently laid on the surface of the brain, and the brain and the electrode were covered with special cover slip, previously fabricated by stacking two 3-mm diameter circular cover slips on a 5-mm one, using transparent optical glue (Loctite Super Glue, dishwasher-resistant). The cranial window was sealed with cyanoacrylate, followed by dental cement. The MEA electrodes were wrapped on the neck of the mouse and unwrapped for the paired imaging/recording session. After the surgery, the mouse underwent meloxicam treatment for 72 hours and fully recovered after 1 week.

Visual stimulation

Visual stimuli were designed using Psychtoolbox-3 (MATLAB), running on a Nvidia GeForce 1060 graphic card, and were presented on a 144-Hz G Sync 27″ monitor, placed frontally, at 18 cm from the eyes of the mouse. Visual stimulation consisted of moving sinusoidal gratings of SF = 0.03 deg^{-1} and TF = 4 Hz, 100% contrast. Stimuli lasted for 4 s, and they were alternated by gray screen presentation, which lasted randomly between 2 to 5 s.

In vivo two-photon imaging, wide-field imaging, and pupillometry

Two-photon imaging data were acquired using an Olympus FVMPE two-photon microscope, equipped with a Ti:Sa laser tuned at 930 nm of excitation. Green fluorescence of GCaMP was collected using a FITC filter and acquired by a conventional PMT (photomultiplier tube) detector. We used a 40× water immersion lens [Olympus; numerical aperture (NA), 0.95]. Laser power on the brain was kept at 35 mW. Data were collected at 30 fps using a resonant galvos. The running setup for the awake mice consisted of a custom-built, floating styrofoam ball on the encoder for locomotory activity. The imaging/electrophysiology session lasted 30 min. Wide-field imaging was performed using a 4× air lens (Olympus; NA, 0.4) and a CMOS (complementary metal-oxide semiconductor) fast camera using a FITC filter in emission (Hamamatsu ORCA Flash 4.0). The online pupillometry measurement was done using a custom-built setup that uses CMUcam5 (Pixy) and open source hardware for the online measurement of pupillometry size and gaze.

In vivo electrophysiology and synchronization

Electrophysiology measurements—together with analog and digital signals from pupillometry, locomotion, microscope triggers, and from the visual stimulation—were recorded from a multichannel acquisition board (Intan RHD2000 acquisition board, Intan RHD2132 32 channel headstage). The ACF cable was connected to the 32-channel headstage with a customized PCB adapter board. Data were acquired at 30 kHz, with a hardware high-pass filter set at 0.1 Hz and a hardware notch filter set at 60 Hz to suppress the contamination from the power line. We used the site closest to the midline of the brain as reference electrode, far from the visual cortex. The ground was connected directly to the titanium head bar.

Data analysis

Imaging data were analyzed as follows: first, data were down-sampled to 10 fps. Then, the images were registered using a bright spot in the image (usually interneurons are bright most of the time) with the image plugin template matching aligner to correct motion artifacts. Then, the regions of interest for each neuron were manually selected on the basis of the autocorrelation image of the video using a lag time of 1 s (GCaMP6s has a decay time of about 1 s). The average fluorescence of each neuron for each frame was measured, and single trace was exported to a customized MATLAB script, which evaluates the basal fluorescence during the moments of no stimulation and calculates the $\Delta F/F$.

Electrophysiology was imported on MATLAB, and we used a customized script to perform the short time fast Fourier transform using a window of 100 ms on each electrode. Then, the 6 × 6 time matrices of the magnitude of the spectrum were generated in the following bands: α (8 to 12 Hz), β (12 to 30 Hz), γ (30 to 50 Hz), high γ (50 to 100 Hz), ultrahigh γ (100 to 300 Hz), and multi-unit (300 Hz to 7 kHz). Other signals, like the sync from the microscope or the analog data

of the pupillometer, were imported to MATLAB and used for fine synchronization and measurement of the arousal of mouse.

Immunohistochemistry

Mice were perfused with cold 4% paraformaldehyde (PFA), and then the brain was explanted and postfixed in PFA for 2 hours at 4°C. Brains were sunk in 10% sucrose in PBS overnight at 4°C, and then sunk in 30% sucrose in PBS overnight at 4°C. The brains were frozen in Tissue-Tek optimum cutting temperature compound and cut into 40-μm coronal sections using a cryostat. The sections were washed three times in PBS, and then incubated in a blocking solution of 5% natural goat serum in PBS-Triton for 2 hours at room temperature. The slices were washed in PBS, and then incubated overnight at 4°C in the primary antibody, which was the Wako anti–Iba-1 rabbit using a 1:750 dilution. After the overnight incubation, slices were washed with PBS three times, and then incubated in the secondary antibody for 2 hours at room temperature. The secondary antibody was the Alexa Fluor 594 goat anti-rabbit used at a dilution of 1:500. The sections were then mounted on slides and coated with DAPI (4′,6-diamidino-2-phenylindole) before being covered and imaged.

Wireless recording with artifact rejection

We have conducted stimulation with simultaneous wireless recording and online artifact rejection to demonstrate the capability of combining nanomesh MEA with custom-designed wireless electronics. The injected stimulus was a biphasic current pulse of 120 μA (reduced to 10 μA for pure Au nanomesh electrodes to accommodate their limited charge capacity) for 200 μs in each phase, and a 100-μs delay between the phases. The stimulation was repeated at a rate of 20 Hz. A stainless steel wire electrode was immersed in the saline solution to inject a neural signal. The neural signal was recorded simultaneously with stimulation by the custom neural recording electronics. The recording circuit can achieve online rejection of artifacts up to 5 V in magnitudes, satisfying the requirement for the largest artifacts that can be safely produced by the nanomesh MEA. The recording with rejected artifact was wirelessly transmitted by the UWB circuit at a data rate of 10 kbps. The used custom UWB design is able to transmit the data wirelessly to a distance up to 1 m at a rate up to 20 Mbps. A custom receiver built from discrete components demodulated the signal to baseband and generated the real-time recorded data stream. The data were captured by an oscilloscope with data acquisition capability and analyzed in MATLAB R2016a.

SUPPLEMENTARY MATERIALS

Supplementary material for this article is available at http://advances.sciencemag.org/cgi/content/full/4/9/eaat0626/DC1

Fig. S1. Bilayer-nanomesh structure and transmittance study.
Fig. S2. Bilayer-nanomesh microelectrode demonstration.
Fig. S3. Impedance results from different bilayer-nanomesh MEAs.
Fig. S4. Bench-top sine wave signal recording.
Fig. S5. Light-induced artifact characterization.
Fig. S6. Demonstration of artifact-free, ITO/PEDOT:PSS bilayer-nanomesh microelectrodes.
Fig. S7. Artifact rejection and wireless recording system.
Fig. S8. Artifact rejection using Au nanomesh microelectrode.
Fig. S9. Histology studies.
Fig. S10. In vivo transparency of MEA.
Fig. S11. Optical imaging underneath microelectrode.
Fig. S12. In vivo impedance measurement after implantation.
Fig. S13. Optimization of nanosphere lithography.
Movie S1. Wide-field epifluorescence of the Ca^{++} indicator GCaMP6s showing the activity in the superficial layers of the mouse visual cortex and the surrounding areas (30× faster than the real time).
Movie S2. Video-rate two-photon Ca^{++} imaging from the neurons of the layer 2/3 of the mouse visual cortex expressing the Ca^{++} indicator GCaMP6s (30× faster than the real time).
Movie S3. Correlation between the $\Delta F/F$ of Ca^{++} wide-field epifluorescence and the MEA recording (30× faster).
Movie S4. The correlated response of arousal (left), the map of the modulation of the power of the MEA recording in different electrophysiology frequency bands (center), and the $\Delta F/F$ of the two-photon Ca^{++} imaging (right) (3× faster than the real time).
Movie S5. Map of the modulation of the power of the MEA recording in the multi-unit band (300 Hz to 7 kHz) during the alternation of visual stimuli and isoluminous gray screen presentations (3× faster than the recording) in which evoked cortical activity (higher, color-coded in red) alternates with spontaneous cortical activity (lower, color-coded in green) based on the stimulus/nonstimulus presentation.

REFERENCES AND NOTES

1. N. Kriegeskorte, R. Goebel, P. Bandettini, Information-based functional brain mapping. *Proc. Natl. Acad. Sci. U.S.A.* **103**, 3863–3868 (2006).
2. M. Scanziani, M. Häusser, Electrophysiology in the age of light. *Nature* **461**, 930–939 (2009).
3. D.-W. Park, A. A. Schendel, S. Mikael, S. K. Brodnick, T. J. Richner, J. P. Ness, M. R. Hayat, F. Atry, S. T. Frye, R. Pashaie, S. Thongpang, Z. Ma, J. C. Williams, Graphene-based carbon-layered electrode array technology for neural imaging and optogenetic applications. *Nat. Commun.* **5**, 5258 (2014).
4. L. Fenno, O. Yizhar, K. Deisseroth, The development and application of optogenetics. *Annu. Rev. Neurosci.* **34**, 389–412 (2011).
5. M. Tsodyks, T. Kenet, A. Grinvald, A. Arieli, Linking spontaneous activity of single cortical neurons and the underlying functional architecture. *Science* **286**, 1943–1946 (1999).
6. J. Viventi, D.-H. Kim, L. Vigeland, E. S. Frechette, J. A. Blanco, Y.-S. Kim, A. E. Avrin, V. R. Tiruvadi, S.-W. Hwang, A. C. Vanleer, D. F. Wulsin, K. Davis, C. E. Gelber, L. Palmer, J. Van der Spiegel, J. Wu, J. Xiao, Y. Huang, D. Contreras, J. A. Rogers, B. Litt, Flexible, foldable, actively multiplexed, high-density electrode array for mapping brain activity in vivo. *Nat. Neurosci.* **14**, 1599–1605 (2011).
7. J. Scholvin, J. P. Kinney, J. G. Bernstein, C. Moore-Kochlacs, N. Kopell, C. G. Fonstad, E. S. Boyden, Close-packed silicon microelectrodes for scalable spatially oversampled neural recording. *IEEE Trans. Biomed. Eng.* **63**, 120–130 (2016).
8. J. J. Jun, N. A. Steinmetz, J. H. Siegle, D. J. Denman, M. Bauza, B. Barbarits, A. K. Lee, C. A. Anastassiou, A. Andrei, Ç. Aydın, M. Barbic, T. J. Blanche, V. Bonin, J. Couto, B. Dutta, S. L. Gratiy, D. A. Gutnisky, M. Häusser, B. Karsh, P. Ledochowitsch, C. Mora Lopez, C. Mitelut, S. Musa, M. Okun, M. Pachitariu, J. Putzeys, P. Dylan Rich, C. Rossant, W.-L. Sun, K. Svoboda, M. Carandini, K. D. Harris, C. Koch, J. O'Keefe, T. D. Harris, Fully integrated silicon probes for high-density recording of neural activity. *Nature* **551**, 232–236 (2017).
9. G. Buzsáki, Large-scale recording of neuronal ensembles. *Nat. Neurosci.* **7**, 446–451 (2004).
10. S. Venkatraman, J. Hendricks, Z. A. King, A. J. Sereno, S. Richardson-Burns, D. Martin, J. M. Carmena, In vitro and in vivo evaluation of PEDOT microelectrodes for neural stimulation and recording. *IEEE Trans. Neural Syst. Rehabil. Eng.* **19**, 307–316 (2011).
11. U. Frey, J. Sedivy, F. Heer, R. Pedron, M. Ballini, J. Mueller, D. Bakkum, S. Hafizovic, F. D. Faraci, F. Greve, K.-U. Kirstein, A. Hierlemann, Switch-matrix-based high-density microelectrode array in CMOS technology. *IEEE J. Solid-State Circuits* **45**, 467–482 (2010).
12. Q. Bai, K. D. Wise, Single-unit neural recording with active microelectrode arrays. *IEEE Trans. Biomed. Eng.* **48**, 911–920 (2001).
13. N. A. Fitzsimmons, W. Drake, T. L. Hanson, M. A. Lebedev, M. A. L. Nicolelis, Primate reaching cued by multichannel spatiotemporal cortical microstimulation. *J. Neurosci.* **27**, 5593–5602 (2007).
14. X. T. Cui, D. D. Zhou, Poly (3,4-ethylenedioxythiophene) for chronic neural stimulation. *IEEE Trans. Neural Syst. Rehabil. Eng.* **15**, 502–508 (2007).
15. R. Balint, N. J. Cassidy, S. H. Cartmell, Conductive polymers: Towards a smart biomaterial for tissue engineering. *Acta Biomater.* **10**, 2341–2353 (2014).
16. J. D. Weiland, D. J. Anderson, Chronic neural stimulation with thin-film, iridium oxide electrodes. *IEEE Trans. Biomed. Eng.* **47**, 911–918 (2000).
17. U. A. Aregueta-Robles, A. J. Woolley, L. A. Poole-Warren, N. H. Lovell, R. A. Green, Organic electrode coatings for next-generation neural interfaces. *Front. Neuroeng.* **7**, 15 (2014).
18. M. D. Ferro, N. A. Melosh, Electronic and ionic materials for neurointerfaces. *Adv. Funct. Mater.* **28**, 1704335 (2017).
19. D. Kuzum, H. Takano, E. Shim, J. C. Reed, H. Juul, A. G. Richardson, J. de Vries, H. Bink, M. A. Dichter, T. H. Lucas, D. A. Coulter, E. Cubukcu, B. Litt, Transparent and flexible low noise graphene electrodes for simultaneous electrophysiology and neuroimaging. *Nat. Commun.* **5**, 5259 (2014).
20. P. Ledochowitsch, E. Olivero, T. Blanche, M. M. Maharbiz, Engineering in Medicine and Biology Society, in *2011 Annual International Conference of the IEEE* (IEEE, 2011), pp. 2937–2940.

21. K. Y. Kwon, B. Sirowatka, A. Weber, W. Li, Opto-μECoG array: A hybrid neural interface with transparent μECoG electrode array and integrated LEDs for optogenetics. *IEEE Trans. Biomed. Circuits Syst.* **7**, 593–600 (2013).
22. N. Kunori, I. Takashima, A transparent epidural electrode array for use in conjunction with optical imaging. *J. Neurosci. Methods* **251**, 130–137 (2015).
23. A. Miyamoto, S. Lee, N. F. Cooray, S. Lee, M. Mori, N. Matsuhisa, H. Jin, L. Yoda, T. Yokota, A. Itoh, M. Sekino, H. Kawasaki, T. Ebihara, M. Amagai, T. Someya, Inflammation-free, gas-permeable, lightweight, stretchable on-skin electronics with nanomeshes. *Nat. Nanotechnol.* **12**, 907–913 (2017).
24. K. J. Seo, Y. Qiang, I. Bilgin, S. Kar, C. Vinegoni, R. Weissleder, H. Fang, Transparent Electrophysiology Microelectrodes and Interconnects from Metal Nanomesh. *ACS Nano* **11**, 4365–4372 (2017).
25. Y. Qiang, K. Jin Seo, X. Zhao, P. Artoni, N. H. Golshan, S. Culaclii, P.-M. Wang, W. Liu, K. S. Ziemer, M. Fagiolini, H. Fang, Bilayer Nanomesh Structures for Transparent Recording and Stimulating Microelectrodes. *Adv. Funct. Mater.* **27**, 1704117 (2017).
26. J. Rivnay, R. M. Owens, G. G. Malliaras, The rise of organic bioelectronics. *Chem. Mater.* **26**, 679–685 (2014).
27. S. J. Wilks, S. M. Richardson-Burns, J. L. Hendricks, D. C. Martin, K. J. Otto, Poly (3,4-ethylenedioxythiophene) as a micro-neural interface material for electrostimulation. *Front. Neuroeng.* **2**, 7 (2009).
28. S. Kellis, K. Miller, K. Thomson, R. Brown, P. House, B. Greger, Decoding spoken words using local field potentials recorded from the cortical surface. *J. Neural Eng.* **7**, 056007 (2010).
29. J. P. Kitzmiller, D. J. Hansford, L. D. Fortin, K. H. Obrietan, V. K. Bergdall, D. Q. Beversdorf, Micro-field evoked potentials recorded from the porcine sub-dural cortical surface utilizing a microelectrode array. *J. Neurosci. Methods* **162**, 155–161 (2007).
30. K. Kostarelos, M. Vincent, C. Hebert, J. A. Garrido, Graphene in the design and engineering of next-generation neural interfaces. *Adv. Mater.* **29**, (2017).
31. W. Yang, A. Broski, J. Wu, Q. H. Fan, W. Li, Characteristics of Transparent, PEDOT: PSS Coated Indium-Tin-Oxide (ITO) Microelectrodes. *IEEE Trans. Nanotechnol.* **17**, (2017).
32. S. F. Cogan, P. R. Troyk, J. Ehrlich, T. D. Plante, D. E. Detlefsen, Potential-biased, asymmetric waveforms for charge-injection with activated iridium oxide (AIROF) neural stimulation electrodes. *IEEE Trans. Biomed. Eng.* **53**, 327–332 (2006).
33. J. D. Weiland, W. Liu, M. S. Humayun, Retinal prosthesis. *Annu. Rev. Biomed. Eng.* **7**, 361–401 (2005).
34. I. R. Minev, P. Musienko, A. Hirsch, Q. Barraud, N. Wenger, E. M. Moraud, J. Gandar, M. Capogrosso, T. Milekovic, L. Asboth, R. F. Torres, N. Vachicouras, Q. Liu, N. Pavlova, S. Duis, A. Larmagnac, J. Vörös, S. Micera, Z. Suo, G. Courtine, S. P. Lacour, Electronic dura mater for long-term multimodal neural interfaces. *Science* **347**, 159–163 (2015).
35. S. Culaclii, B. Kim, Y.-K. Lo, L. Li, W. Liu, Online artifact cancelation in same-electrode neural stimulation and recording using a combined hardware and software architecture. *IEEE Trans. Biomed. Circuits Syst.* **12**, 601–613 (2018).
36. Y.-K. Lo, K. Chen, P. Gad, W. Liu, A fully-integrated high-compliance voltage SoC for epi-retinal and neural prostheses. *IEEE Trans. Biomed. Circuits Syst.* **7**, 761–772 (2013).
37. M. S. Chae, Z. Yang, M. R. Yuce, L. Hoang, W. Liu, A 128-channel 6 mW wireless neural recording IC with spike feature extraction and UWB transmitter. *IEEE Trans. Neural Syst. Rehabil. Eng.* **17**, 312–321 (2009).
38. G. J. Goldey, D. K. Roumis, L. L. Glickfeld, A. M. Kerlin, R. C. Reid, V. Bonin, D. P. Schafer, M. L. Andermann, Long-term imaging in awake mice using removable cranial windows. *Nat. Protoc.* **9**, 2515–2538 (2014).
39. S. S. Sato, P. Artoni, S. Landi, O. Cozzolino, R. Parra, E. Pracucci, F. Trovato, J. Szczurkowska, S. Luin, D. Arosio, F. Beltram, L. Cancedda, K. Kaila, G. Michele Ratto, Simultaneous two-photon imaging of intracellular chloride concentration and pH in mouse pyramidal neurons in vivo. *Proc. Natl. Acad. Sci. U.S.A.* **114**, E8770–E8779 (2017).
40. T.-W. Chen, T. J. Wardill, Y. Sun, S. R. Pulver, S. L. Renninger, A. Baohan, E. R. Schreiter, R. A. Kerr, M. B. Orger, V. Jayaraman, L. L. Looger, K. Svoboda, D. S. Kim, Ultrasensitive fluorescent proteins for imaging neuronal activity. *Nature* **499**, 295–300 (2013).
41. M. Vinck, R. Batista-Brito, U. Knoblich, J. A. Cardin, Arousal and locomotion make distinct contributions to cortical activity patterns and visual encoding. *Neuron* **86**, 740–754 (2015).
42. M. J. McGinley, S. V. David, D. A. McCormick, Cortical membrane potential signature of optimal states for sensory signal detection. *Neuron* **87**, 179–192 (2015).
43. V. Porciatti, T. Pizzorusso, L. Maffei, The visual physiology of the wild type mouse determined with pattern VEPs. *Vision Res.* **39**, 3071–3081 (1999).

Acknowledgments: We thank the cleanroom staff of George J. Kostas Nanoscale Technology and Manufacturing Research Center at Northeastern University for technical support. **Funding:** This work was supported by Northeastern University, NIH National Institute of Neurological Disorders and Stroke (R01NS095959), Rettsyndrome.org, Rett Syndrome Research Trust, Simon Foundation, Human Frontier Science Program–Cross-Disciplinary Fellowships, World Premier International Research Initiative–International Research Center for Neurointelligence (Japan Society for the Promotion of Science) [WPI-IRCN (JSPS)], Endowment for the Chan Soon-Shiong Bionic Engineering Research Center, and University of California, Los Angeles. We would like to thank The Endowment of California Capital Equity LLC for their partial support in the system research. **Author contributions:** Y.Q., K.J.S., P.A., M.F., and H.F. designed the research. Y.Q., K.J.S., Y.Z., X.Z., X.H., Y.L., H.A.P., and Y.H. fabricated the devices and electronics. Y.Q., P.A., K.J.S., X.Z., and Y.L. performed the data analysis. P.A., V.H., and Y.Q. carried out the in vivo experiments. S.C., P.-M.W., Y.-K.L., and W.L. performed the stimulation artifacts rejection and wireless recording. A.S. and J.S.V.C. conducted the experiments to optimize nanosphere lithography. Y.Q., P.A., K.J.S., S.C., W.L., M.F., and H.F. co-wrote the manuscript. **Competing interests:** W.L. and Y.-K.L. are inventors on a patent application related to this work filed by the Regents of the University of California (U.S. application no. US20170273594A1 and WO application no. WO2016057244A1; priority date, 10 October 2014). All the other authors declare that they have no competing interests. **Data and materials availability:** All data needed to evaluate the conclusions in the paper are present in the paper and/or the Supplementary Materials. Any additional data sets, analysis details, and material recipes are available upon request.

Submitted 19 January 2018
Accepted 24 July 2018
Published 5 September 2018
10.1126/sciadv.aat0626

Citation: Y. Qiang, P. Artoni, K. J. Seo, S. Culaclii, V. Hogan, X. Zhao, Y. Zhong, X. Han, P.-M. Wang, Y.-K. Lo, Y. Li, H. A. Patel, Y. Huang, A. Sambangi, J. S. V. Chu, W. Liu, M. Fagiolini, H. Fang, Transparent arrays of bilayer-nanomesh microelectrodes for simultaneous electrophysiology and two-photon imaging in the brain. *Sci. Adv.* **4**, eaat0626 (2018).